Journal of the Mechanical Behavior of Biomedical Materials 181 (2026) 107486



Contents lists available at ScienceDirect

Journal of the Mechanical Behavior of Biomedical Materials

journal homepage: www.elsevier.com/locate/jmbbm



Distinguishing cancerous from non-malignant breast cells using viscoelastic creep and functional principal component analysis

Jolene Cao [a], Killian Onwudiwe [b], Jingjie Hu [c], Meenal Datta [b], Wole Soboyejo [d,*]

[a] Department of Statistics, Harvard University, 33 Oxford Street, Cambridge, MA, 02138, USA
[b] Department of Aerospace and Mechanical Engineering, University of Notre Dame, 365 Fitzpatrick Hall of Engineering, Notre Dame, IN, 46556, USA
[c] Department of Mechanical and Aerospace Engineering, North Carolina State University, P. O. Box 7910, Raleigh, NC, 27695, USA
[d] Department of Engineering, SUNY Polytechnic Institute, 100 Seymour Rd, Utica, NY, 13502, USA

ARTICLE INFO

Keywords:
Cancer detection
Triple-negative breast cancer
Cell mechanics
Microfluidics
Fluid shear stress
Creep compliance
Time series data
Nuclei
Cytoplasm
Cytoskeleton
Data science

ABSTRACT

The mechanical responses and properties of breast epithelial cells are known to change during malignant transformation and progression due to the dynamics of their actin cytoskeleton network organization and the resulting viscoelastic deformability. Studying the viscoelastic creep behavior of breast cells may reveal new avenues for developing novel cancer diagnostic and therapeutic biomarkers and improving fundamental biophysical understanding of the disease. Here we present an approach that uses functional principal component analysis (fPCA) to distinguish between the viscoelastic responses of malignant and non-malignant live breast cells that are subjected to shear flow in microfluidic channels under *in-situ* observation with optical, fluorescence, and confocal microscopy. The fPCA method extracts critical features of cell viscoelasticity from the *in-situ* measured creep responses of non-tumorigenic breast cells (MCF-10A), less metastatic triple-negative breast cancer (TNBC) cells (MDA-MB-468), and highly metastatic breast cancer cells (MDA-MB-231). The results demonstrate distinguishable clustering patterns for the three types of cells in the first principal component (PC) and the second PC space. The first PC, indicative of the overall level of creep compliance, accounts for more than 98% of the total variance in the observed creep responses. The scores of the cells examined on the first PC axis increase with increasing cancer malignancy. They also correlate highly with the average moduli and viscosities extracted from viscoelastic models (−83% correlation with moduli and −85% correlation with viscosities). This suggests a direct link between the malignancy of cancer and the overall creep compliance level that is governed by cell viscoelastic properties. The implications of the results are discussed for the detection of non-tumorigenic and tumorigenic breast cells at different stages of cancer progression.

1. Introduction

Tumor cells within the human body experience various mechanical forces, including shear stresses due to fluid flow in blood vessels and other tissues (Jain et al., 2014; Zhang et al., 2022). Understanding the mechanical responses of live cells subjected to shear flow is crucial for advancing our knowledge of tumor biology (Jain et al., 2014; Liu et al., 2021). It also accelerates drug development and enables the creation of more effective, personalized cancer diagnostics and therapies, including microfluidic tumor-on-a-chip systems (Liu et al., 2021; Moccia and Haase, 2021; Zhang et al., 2022).

Cell viscoelasticity plays a critical role in cells' responses under flow conditions. When cells are subjected to shear flow, the shear stress can induce cytoskeletal rearrangements and its associated viscoelastic deformability, leading to changes in cell shape and migration behavior. A number of studies have focused on cell viscoelasticity using various techniques such as atomic force microscopy (Wu et al., 1998; Calzado-Martin et al., 2016; Ketene et al., 2012), embedded particle tracking (Wirtz et al., 2009; Tseng et al., 2002), laser tracking microrheology (Yamada et al., 2000), and micropipette aspiration (Guilak et al., 2000; Dao et al., 2003; Nagelkerke et al., 2015). However, these techniques often damage the intracellular structure of the cell and, therefore, introduce uncertainty for the measurements.

In contrast, we have studied the mechanical responses of live cells at progressive stages of cancer malignancy under shear flow *in-situ* and revealed many unique insights into cells' actin cytoskeleton network

* Corresponding author.
E-mail address: soboyew@sunypoly.edu (W. Soboyejo).

https://doi.org/10.1016/j.jmbbm.2026.107486
Received 3 January 2024; Received in revised form 3 February 2025; Accepted 27 May 2026
Available online 27 May 2026
1751-6161/© 2026 Published by Elsevier Ltd.

organization and the resulting viscoelastic deformability (Cao et al., 2006; Hu et al., 2018; Ani et al., 2019; Onwudiwe et al., 2021). However, our prior studies use a viscoelastic modeling framework to extract cell mechanical properties. They rely heavily on human judgment to decide the primary deformation regime, model selection, and nonlinear fitting parameters to address potential convergence problems (Cao et al., 2006; Hu et al., 2018; Onwudiwe et al., 2021).

Unbiased data science techniques that do not rely on strong assumptions regarding the underlying data have developed rapidly in the "big data" revolution to help extract hidden patterns in cell biology (Lähnemann et al., 2020). This approach tends to be less subjective and more automatable in learning complex relationships in many cell biology research areas such as single-cell omics, diagnosis, and imaging (Ji et al., 2021; Mayro et al., 2020; Driscoll and Zaritsky, 2021).

Functional principal component analysis (fPCA), as a novel and important tool in data science (Wang et al., 2016; Aneiros et al., 2019), can better analyze time series data such as the temporal mechanical responses of cells under shear stress, and therefore, can offer new opportunities and perspectives for extracting critical features of cell viscoelastic behavior in a more objective, automatic, and data-driven way.

In this paper, a new approach to breast cancer detection by combining fPCA, a powerful technique to extract valuable information from time series, with established shear assay experiments and digital image correlation (DIC) measurements is reported. The study focuses on shear assay data obtained from non-tumorigenic breast cells, less metastatic triple-negative breast cancer cells, and highly metastatic breast cancer cells. The results demonstrate distinguishable clustering patterns for the three types of cells in the first principal component (PC) - second PC space. The first PC representing the overall creep compliance level captures a dominant portion of the total explained variance (>98%) for all the investigated sample sets, indicating it could be a major factor to consider for differentiating different cancer malignancies.

The first PC scores of MCF-10A normal breast cells, less metastatic MDA-MB-468 TNBC cells, and highly metastatic MDA-MB-231 TNBC cells show an increasing trend, 83% negatively correlated with the average moduli and 85% negatively correlated with the average viscosities reported in the prior research using a viscoelastic modeling curve fitting approach for these same three cell lines. This suggests that cancer malignancy is directly correlated with cell overall creep compliance level, which is determined by cell viscoelasticity.

2. Experimental methods

In this paper, non-tumorigenic breast cells (MCF-10A), less metastatic breast cancer cells (MDA-MB-468), and highly metastatic breast cancer cells (MDA-MB-231) were studied via cell culture, immunofluorescence staining, confocal microscopy, and fluid shear stress assay techniques as previously reported by our group (Cao et al., 2006; Hu et al., 2018; Ani et al., 2019; Onwudiwe et al., 2021; Holen et al., 2023).

2.1. Sample preparation

The normal breast cell line, MCF-10A (ATCC# CRL-10317), the less metastatic breast cell line, MDA-MB-468 (ATCC# HTB-132), and the highly metastatic breast cell line, MDA-MB-231 (ATCC# HTB-26), were cultured following the protocols outlined in previous investigations (Hu et al., 2018; Onwudiwe et al., 2021). For a duration of 48 h, the cells were cultured in 60 × 15 × 35 mm Falcon Petri dishes (Corning Inc., Corning, NY), maintaining a controlled environment at 37 °C with 5% CO2 concentration under standard atmospheric pressure. This ensured optimal cell attachment and growth on the substrate.

Under these controlled conditions, the MCF-10A cells were cultured using a blend of Dulbecco's modified Eagle's medium (DMEM) and Ham's F-12 medium (Invitrogen, Carlsbad, CA) at a 1:1 mix ratio. The culture medium was supplemented with 5% horse serum (Invitrogen, Carlsbad, CA), 0.2% amphotericin (Gemini Bio-Products, West Sacramento, CA), 30 ng/ml insulin (Sigma-Aldrich, St. Louis, MO), 100 ng/ml cholera toxin (Sigma Aldrich), 30 ng/ml murine epidermal growth factor (PeproTech), 0.5 μg/ml hydrocortisone (Sigma Aldrich), and 1% Penicillin-Streptomycin (Invitrogen, Carlsbad, CA). The MDA-MB-468 and MDA-MB-231 cells were cultured under the same controlled conditions, utilizing 10% fetal bovine serum from the American Type Culture Collection (ATCC), Manassas, VA, along with L-15 base media. The culture medium for MDA-MB-468 and MDA-MB-231 cells also contained supplemented 100 I.U./ml penicillin and 100 μg/ml streptomycin, respectively.

The variations in the densities of actin cytoskeleton between the cells were examined using immunofluorescence staining and confocal microscopy imaging techniques as previously reported by our group (Hu et al., 2018; Onwudiwe et al., 2021).

2.2. Shear assay experiments

The modified shear assay technique was previously reported by our group (Cao et al., 2006; Hu et al., 2018), and the visualized detail of the experiment was also reported (Holen et al., 2023).

Fig. 1 shows the schematics of the shear assay experimental setup and the cross-section view of a cell under shear assay laminar flow. The monitoring system of an optical microscope (Nikon Instruments Inc., Melville, NY, USA) and video camera (INFINITY2-1R, Lumenera Corporation, Ottawa, ON, Canada) was used to observe and record individual cells being deformed under shear flow *in-situ*.

The Reynolds number was calculated to be on the order of one or less, thus permitting laminar flow. The wall shear stress at the wall of the flow chamber τ was determined as below (Vankooten et al., 1992; Cooke et al., 1993):

$$\tau = \frac{6\mu Q}{wh^2} \tag{1}$$

where Q represents the volumetric flow rate, μ represents the media viscosity, w and h are the width and height of the chamber, respectively.

Note the cells, after a cycle of experiment, were discarded. During each shear assay experiment, the cells eventually detached from the underlying extracellular matrix (ECM) on the substrate and flew out of the shear assay system. Discarding cells after each experiment can ensure fresh cells without damage to their intracellular structures were

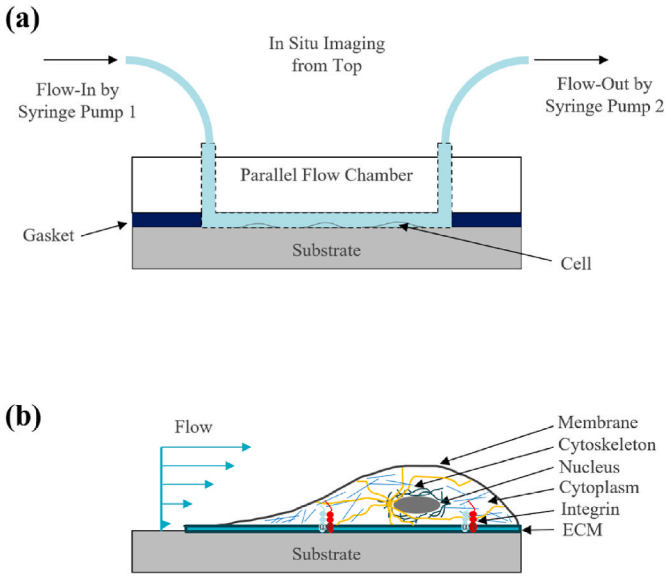


Fig. 1. (a) Schematics of shear assay experimental setup and (b) cross-section view of a cell under shear assay laminar flow.

used, therefore minimizing the measurement uncertainty.

A major challenge in the shear assay experiments was getting accurate quantitative information on local strains during cell deformation before the onset of cell failure/detachment. Well-controlled laminar flow conditions were designed to apply appropriate shear stress so that the *in-situ* imaging system can capture sufficient cell deformation data before cell detachment. A digital image correlation technique was used to map out the displacement and strain field using the collected cell deformation *in-situ* images.

3. Modeling

3.1. Digital image correlation technique

Digital Image Correlation (DIC) techniques (Pan et al., 2009; Krehbiel et al., 2010; Pan, 2018; Yang and Bhattacharya, 2019; Takada et al., 2023) were used to analyze the time-dependent deformation of points within the cells during the shear assay test. It measures the displacements by sequentially matching subset pixel patterns in the recorded reference and deformed images using correlation functions.

Once the displacement field (u, v) is determined after DIC and the associated postprocessing improvements such as smoothing, the displacement gradients $\left(\frac{\partial u}{\partial x}, \frac{\partial u}{\partial y}, \frac{\partial v}{\partial x}, \frac{\partial v}{\partial y}\right)$ can be calculated to derive the strain field. The two-dimensional Lagrangian finite strain tensor components $(\varepsilon_{xx}, \varepsilon_{yy}, \varepsilon_{xy})$ are given below to calculate strains assuming the deformation is predominantly in-plane (Chu et al., 1985):

$$\varepsilon_{xx} = \frac{\partial u}{\partial x} + \frac{1}{2}\left[\left(\frac{\partial u}{\partial x}\right)^2 + \left(\frac{\partial v}{\partial x}\right)^2\right] \tag{2}$$

$$\varepsilon_{yy} = \frac{\partial u}{\partial y} + \frac{1}{2}\left[\left(\frac{\partial u}{\partial y}\right)^2 + \left(\frac{\partial v}{\partial y}\right)^2\right] \tag{3}$$

$$\varepsilon_{xy} = \frac{1}{2}\left(\frac{\partial u}{\partial y} + \frac{\partial v}{\partial x}\right) + \frac{1}{2}\left(\frac{\partial u}{\partial x}\frac{\partial u}{\partial y} + \frac{\partial v}{\partial x}\frac{\partial v}{\partial y}\right) \tag{4}$$

DaVis software (LaVision, Göttingen, Germany) was used in this study to calculate displacements and strains. A step size of 1.4 μm (8 pixels) and subset size of 5.5 μm × 5.5 μm were selected for the correlation optimization process, where each subset of pixels is sequentially scanned to search for the best-correlated patterns.

3.2. Viscoelastic deformation

Viscoelastic properties of cells and tissue (Matthews et al., 2004; Forgacs et al., 1998) have been characterized using various viscoelastic models based on different combinations of the linear elastic spring and the linear viscous dash-pot. All these linear viscoelastic models follow a linear viscoelastic constitutive equation of the general form below:

$$p_0\sigma + p_1\dot{\sigma} + p_2\ddot{\sigma} + p_3\dddot{\sigma} + \ldots = q_0\varepsilon + q_1\dot{\varepsilon} + q_2\ddot{\varepsilon} + q_3\dddot{\varepsilon} + \ldots \tag{5}$$

where σ is the stress, ε is the strain, $\dot{\sigma}$, $\ddot{\sigma}$, $\dddot{\sigma}$ are the 1st, 2nd, and 3rd order of time derivates of stress, $\dot{\varepsilon}$, $\ddot{\varepsilon}$, $\dddot{\varepsilon}$ are the 1st, 2nd, and 3rd order of time derivates of strain, and p_0 , p_1 , p_2 , p_3 , q_0 , q_1 , q_2 , q_3 are the corresponding coefficients. The more springs and dashpots that are used in the viscoelasticity model, the more material parameters that need to be determined, and the higher order this differential equation will be.

In this study, the viscoelastic cell deformation under constant shear stress τ_0 can be modeled as a viscoelastic creep process, where creep compliance $C_{creep}(t)$ is typically used to characterize the material strain subjected to unit stress as below:

$$C_{creep}(t) = \frac{\varepsilon(t)}{\tau_0} \tag{6}$$

Creep compliance $C_{creep}(t)$ data were used in the current investigation of cell viscoelastic behavior using fPCA.

The results were compared to the viscoelastic material parameters extracted in our prior research of breast cell viscoelasticity using a 3-element generalized Maxwell viscoelastic model in Fig. 2. Note the creep response before removing the constant stress in Fig. 2(b) represents a specific version of Eq. (5). In this version of viscoelastic model, three viscoelastic parameters (shear modulus E, viscosities η_1 and η_2) can be obtained by fitting the model to the creep compliance versus time data obtained from the experiments.

3.3. Functional principal component analysis

FPCA has become a key dimension reduction tool for functional data such as time series since its discovery (Wang et al., 2016; Aneiros et al., 2019). Its popularity is attributed to its capability of converting inherently infinite-dimensional functional data (e.g. the creep compliance time series data in the current study) to a finite-dimensional vector of scores with strong explanatory power. Therefore, powerful dimension reduction can be accomplished, and conventional multivariate data analysis can be readily used in the resulting low-dimensional space defined by the top PCs.

The sample curves $x_i(t), i = 1, \ldots, n$ of a time series process $X(t)$ can be expressed as below using the Karhunen-Loève expansion (Wang et al., 2016):

$$x_i(t) = \mu(t) + \sum_{k=1}^{\infty} A_{ik}\varphi_k(t) \tag{7}$$

where $t \in \mathrm{I}$, $\mu(t)$ is the mean of $X(t)$, $\varphi_k(t)$ is the PC in the k-th dimension, and A_{ik} is the corresponding score of $x_i(t)$ projected to the k-th dimension PC.

It can be proved that the PCs $\varphi_k(t)$ are the eigenfunction of the covariance function $G(s,t) = Cov(X(s), X(t))$ corresponding to the eigenvalue λ_k and will satisfy below conditions:

$\int \varphi_k^2(t)dt = 1$ and $\int \varphi_j(t)\varphi_k(t)dt = 0$ for any $j \neq k$. The PC scores A_{ik}

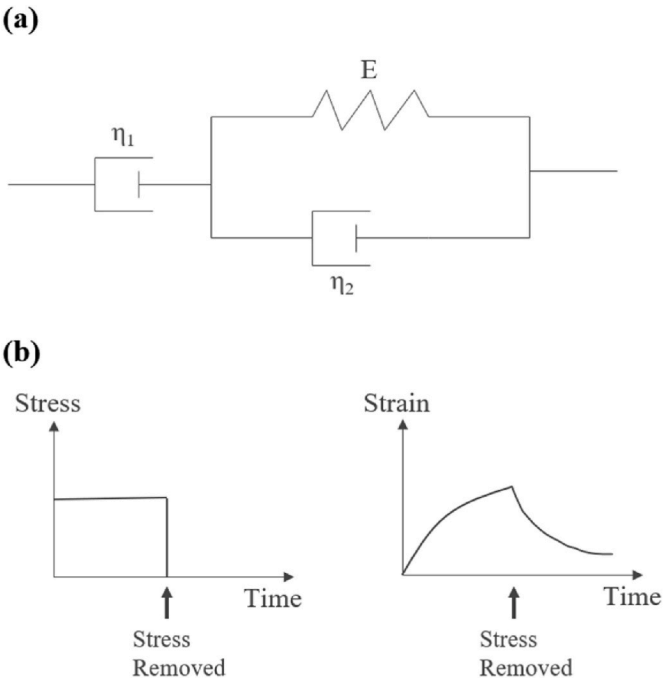


Fig. 2. (a) Schematics of a 3-element generalized Maxwell viscoelastic model used for shear assay experiments and (b) its time-dependent creep recovery strain response produced by applying constant stress followed by removing the stress.

can be calculated as:

$$A_{ik} = \int_I (x_i(t) - \mu(t))\varphi_k(t)dt \tag{8}$$

When the first K PCs can explain most the variability in the sample curves, the first K terms can be used as below to approximate the infinite sum in Eq. (7):

$$x_{iK}(t) = \mu(t) + \sum_{k=1}^{K} A_{ik}\varphi_k(t) \tag{9}$$

where $x_{iK}(t)$ is the approximated process of $x_i(t)$ using the first K PCs. Therefore, the information contained in the original sample curves $x_i(t)$ is now essentially contained in the scores $(A_{i1}, \ldots, A_{iK})$ of the finite K-dimensional space expanded by the first K PCs. At least 85% of variability explained using the first K PCs was typically suggested to select the value of K by prior research (Li et al., 2014; Sang et al., 2017).

4. Results and discussion

4.1. Cell deformation and strain temporal variations

Cell deformation patterns under controlled laminar flow were captured by sequentially correlating the recorded *in-situ* cell images using DIC. Typical analyzed image sequences are presented in Fig. 3, where the displacement field of an MCF-10A normal breast cell during a shear assay experiment with the calculated wall shear stress of 400 Pa is shown. It shows significant initial deformation starts along the periphery of the cell in Fig. 3(b), then the deformation gradually propagates to a more central area by a non-uniform progression in Fig. 3(c)–(d). The cell center area remains at relatively low deformation in Fig. 3(e)–(g), though the low-level deformation area is shrinking, and eventually, all cell areas reach a high level of displacement as shown in Fig. 3(h).

The series of images in Fig. 3(a)–(h) might indicate center nucleus region has a higher stiffness than the more peripheral cell cytoplasm region, which deforms first. This is consistent with the prior cell modulus studies (Cao et al., 2006; Hu et al., 2018; Onwudiwe et al., 2021; Holen et al., 2023) in which higher cell modulus was observed at the cell nucleus region compared to the cytoplasm region.

Strain field can be calculated from the displacement map given by DIC, using the Lagrangian finite strain tensor as shown in Eqs. (2)–(4). Representative shear strain versus time data was plotted in Fig. 4(a), which shows three-stage creep behavior as reported in a prior study (Hu et al., 2018). This creep behavior includes an initial linear viscoelastic deformation primary regime, a relatively small slope secondary regime

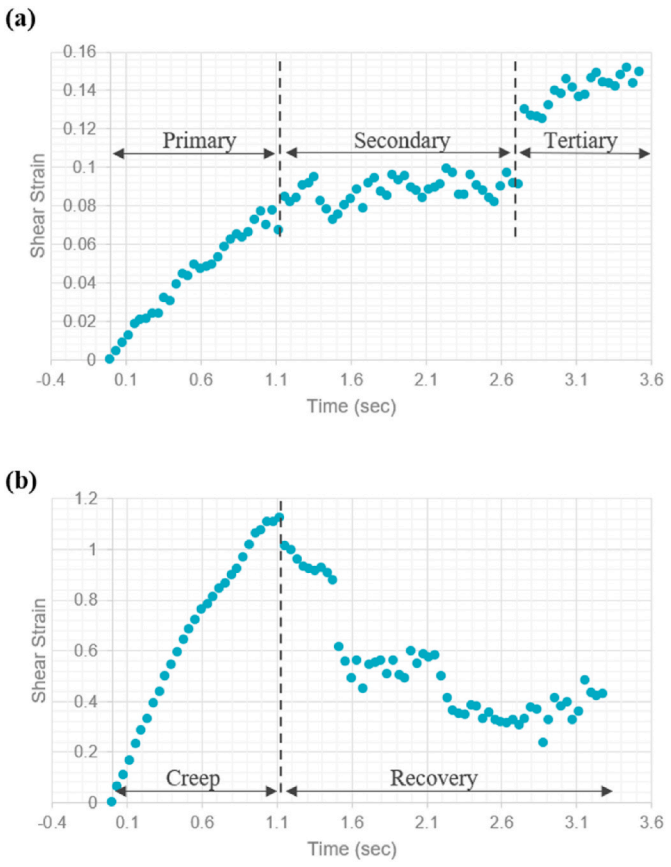


Fig. 4. Shear strain versus time curves showing (a) representative primary, secondary, and tertiary three-stage creep behavior for the nucleus region of a less metastatic MDA-MB-468 breast cancer cell and (b) typical viscoelastic creep-recovery response as illustrated in Fig. 2(b).

with some viscoelasticity nonlinearity, and a last tertiary stage with rapidly increasing strain before cell detachment from the substrate. Linear viscoelastic modeling using specific versions of Eq. (5) to extract cell mechanical properties typically focuses on the initial primary regime, which is clearly distinguishable in Fig. 4(a).

Though it is noticed that three-stage creep behavior is not always clearly distinguishable. This would make the use of traditional viscoelastic models challenging due to the difficulty to identify the initial primary regime. Fig. 4(b) represents a complete creep-recovery process

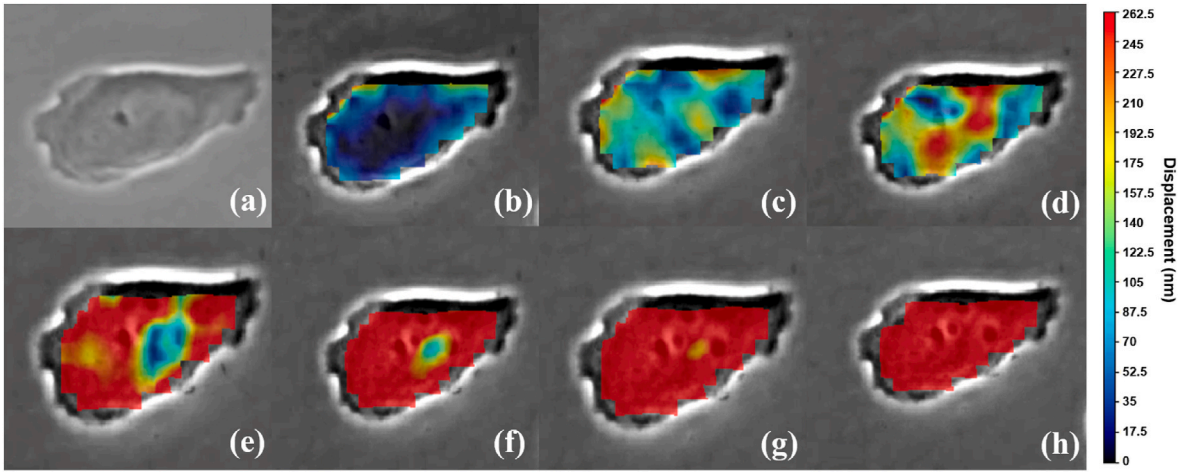


Fig. 3. Image sequences captured for an MCF-10A normal breast cell during a shear assay experiment with the calculated wall shear stress of 400 Pa.

of the nucleus region of a less metastatic MDA-MB-468 breast cancer cell subject to shear flow until after its detachment from the substrate.

The creep part of the curve exhibits the three-stage creep behavior but to a much less degree and the linear viscoelasticity regime for modeling is not clearly distinguishable to be separated out. It might be required to assume negligible nonlinear viscoelasticity here in order to properly model the collected data. Fitting a carefully selected linear viscoelastic model such as the 3-element generalized Maxwell model illustrated in Fig. 2(a) to either the creep part or the complete creep-recovery process would help extract cell moduli and viscosities given the negligible nonlinear viscoelasticity assumption. Modern data science-based fPCA was used next to avoid these challenges in model assumption and model selection using traditional linear viscoelasticity modeling approach.

4.2. Functional principal component analysis

4.2.1. Creep compliance - time data smoothing

K-nearest neighbor (k-NN) algorithm-based kernel smoothing was used to smooth the creep compliance-time data in an effort to minimize potential undesired impacts from random data noises that could be due to shear assay imaging/DIC measurement errors or inherent system noise. The as-collected creep compliance versus time data of MCF-10A normal breast cells and its smoothed version after k-NN kernel smoothing are shown in Fig. 5(a) and (b), respectively. The number of neighbors was selected from values 2, 3, 4, and 5 by an optimization process based on Shibata's model selection criterion (Hurvich et al., 1989).

4.2.2. Functional principal components

Table 1 summarizes the variance explained by the top four PCs for different sample sets in the investigation. It is obvious that the first PC dominantly explains the variance (above 98%) in the creep compliance data. The second PC can be another component that explains significant variance (around 1%). The other PCs seem trivial as they could only explain less than 0.4% variance each. Therefore, most of the information contained in the data should be mainly represented by the first and second PCs. This dimension reduction process could significantly simplify subsequent analysis because only the top two components would be needed.

The first to fourth PCs were calculated for different sample sets. Typical top PCs and the corresponding harmonics and models, in terms of how they are superimposed to the mean creep compliance function, are provided in Fig. 6. PC1 in Fig. 6(a) is positive for all the time with a monotonically increasing trend, representing the overall level of creep compliance deviation from the creep compliance mean function but with an increasing degree of deviation when the time increases.

The mode of this first PC can be clearly observed in Fig. 6(b), where the mean creep compliance function plus or minus the first PC is shown. The PC2 curve in Fig. 6(a) crosses the zero axis once from the positive creep compliance regime to the negative regime with a different trend on either side, which could be interpreted as the contrast of earlier creep compliance versus later creep compliance relative to the mean function. Fig. 6(c) clearly shows how this secondary mode makes individual creep compliance curves deviating from the mean creep compliance curve. Though the contribution of the second PC mode is very limited due to its much smaller explained variance (1%) compared to the explained variance for the first PC (98%).

The interpretations of PC3 and PC4 and their modes are not the focus of this study, due to their negligible explained variance (in total).

Table 1
Variance explained by the top four PCs - PC1, PC2, PC3, and PC4 for different sample sets. n = 897 for the sample set of nucleus and cytoplasm; n = 433 for the sample set of nucleus only; n = 464 for the sample set of cytoplasm only.

Functional Principal Components	Sample Sets Used		
	Nucleus + Cytoplasm	Nucleus Only	Cytoplasm Only
	MCF-10A MDA-MB-468 MDA-MB-231	MCF-10A MDA-MB-468 MDA-MB-231	MCF-10A MDA-MB-468 MDA-MB-231
PC1	98.30%	98.39%	98.24%
PC2	1.10%	1.08%	1.16%
PC3	0.38%	0.32%	0.37%
PC4	0.12%	0.13%	0.12%

4.2.3. Clustering based on functional principal component scores

The first PC and the second PC scores of each measured creep compliance curve can be used as Cartesian coordinates to construct the score plots as shown in Fig. 7, which is based on the creep compliance data up to 0.4 s for the three investigated cell types. These score plots show distinguishable clusters of MCF-10A normal breast cells with less metastatic MDA-MB-468 TNBC cells, and highly metastatic MDA-MB-231 TNBC cells. Note PCs were calculated using both nucleus and cytoplasm data in Fig. 7(a)–(b), nucleus data only in Fig. 7(c), and cytoplasm data only in Fig. 7(d). Scores of cytoplasm and nucleus regions in Fig. 7(a) were separately displayed in Fig. 7(b). Fig. 7 shows that the clusters of MCF-10A normal breast cells and less metastatic MDA-MB-468 TNBC cells are clearly different from those of highly metastatic MDA-MB-231 TNBC cells in terms of cluster size, density, and center position. Both MCF-10A normal breast cell clusters and less metastatic MDA-MB-468 TNBC cell clusters have smaller sizes, more density, and more proximity to the lower values of PC1 than those of highly metastatic MDA-MB-231 TNBC cells. Though the difference between MCF-10A normal breast cells and less metastatic MDA-MB-468 TNBC cells is much smaller and less distinguishable, indicating potential challenges in early cancer detection.

Since PC1 scores represent the main level of creep compliance, the order of the clusters of MCF-10A normal breast cells, less metastatic MDA-MB-468 TNBC cells, and highly metastatic MDA-MB-231 TNBC cells along the PC1 axis shows that MCF-10A normal breast cells have the highest stiffness, highly metastatic MDA-MB-231 TNBC cells have

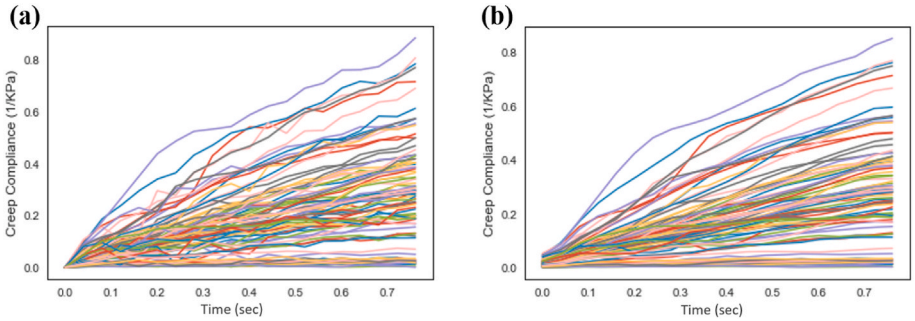


Fig. 5. Creep compliance versus time data of MCF-10A normal breast cells (a) as-collected and (b) after smoothing using a k-nearest neighbor algorithm.

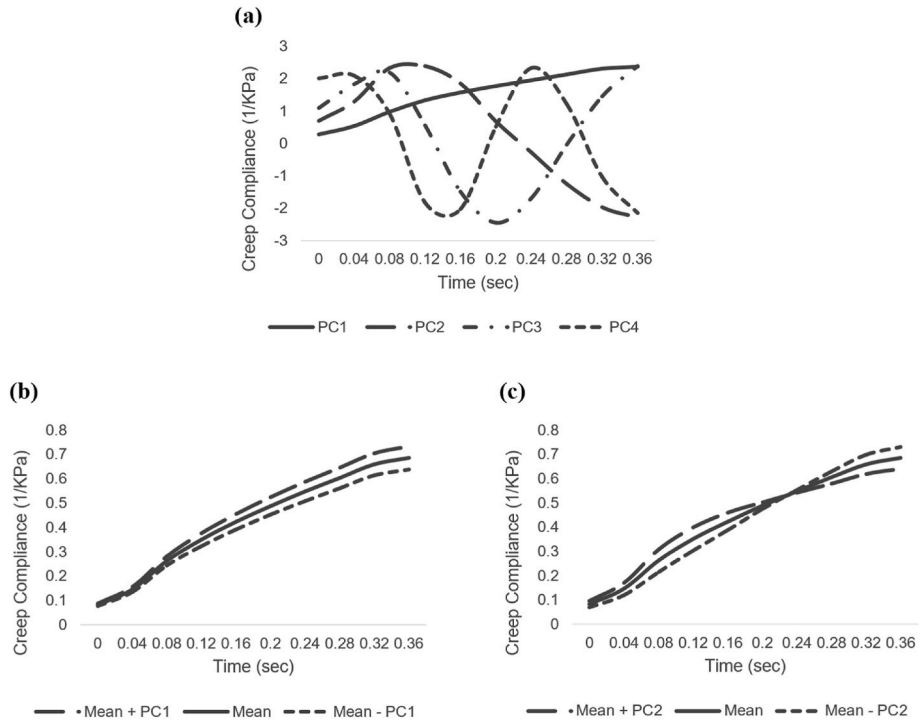


Fig. 6. Top PCs and the corresponding harmonics/modes using nucleus and cytoplasm creep compliance data of MCF-10A, MDA-MB-468 and MDA-MB-231 cells: The top four PCs PC1, PC2, PC3, and PC4 in (a); The harmonics/modes of PC1 and PC2 in (b) and (c), respectively, where the mean function (solid curve) ± corresponding PCs are shown.

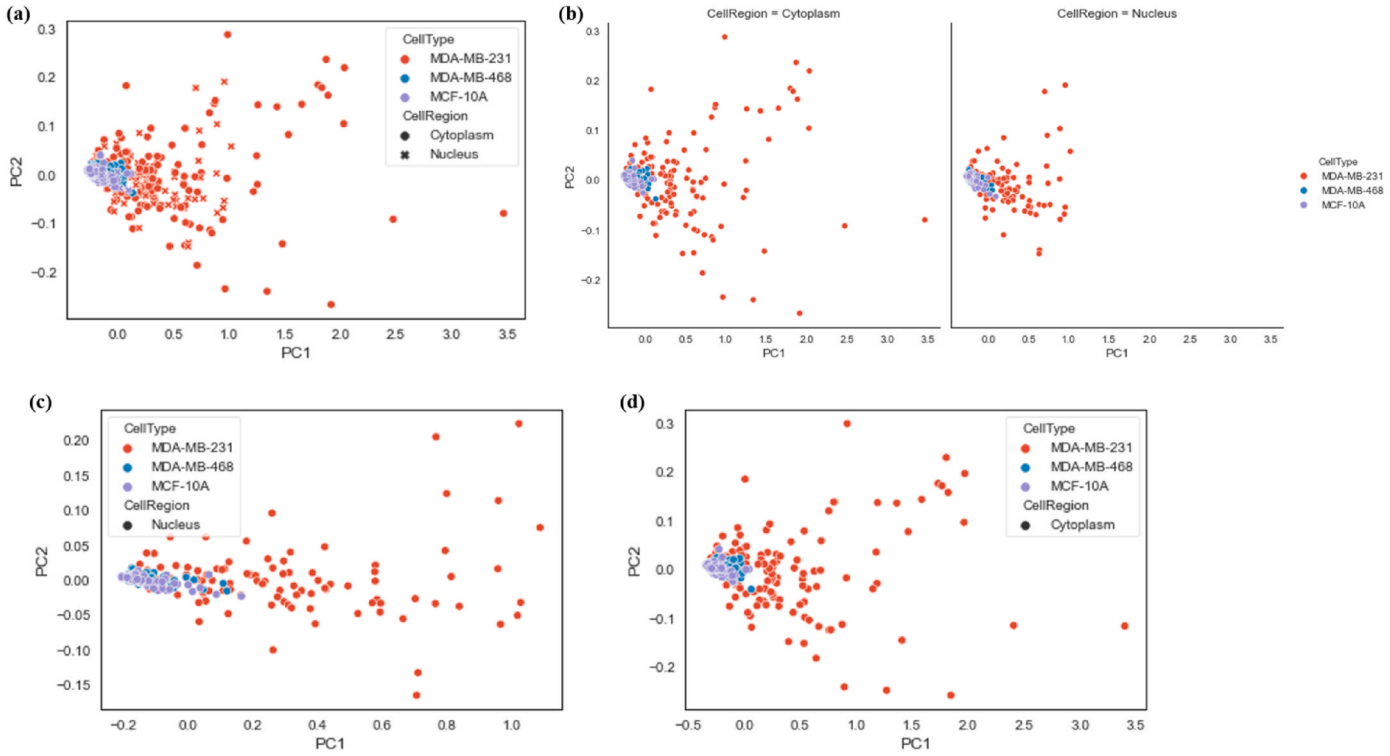


Fig. 7. FPCA score plots on PCs where PC1 and PC2 are constructed using creep compliance data up to 0.4 s for all three cell types. (a) both nucleus and cytoplasm data used and displayed together, (b) both nucleus and cytoplasm data used but displayed separately, (c) only nucleus data used, and (d) only cytoplasm data used.

the smallest stiffness, and less metastatic MDA-MB-468 TNBC cells are between, though with significant overlapping with the MCF-10A normal breast cells. This might suggest that cancer malignancy state could be detected from simple score plots directly based on creep compliance data from *in-situ* cell shear assay. The finding on cell stiffness from the perspective of cluster size, density, and center position in the PC1-PC2 space is consistent with earlier reported shear modulus and viscosity measurements for these three types of cells (Hu et al., 2018; Onwudiwe

et al., 2021; Holen et al., 2023).

Fig. 7 also shows that score plots constructed from PCs that were calculated using either all nucleus and cytoplasm data, or only nucleus data, or only cytoplasm data show similar discrimination power for the three investigated breast cell types. This confirms highly metastatic MDA-MB-231 TNBC cells are mechanically significantly different from the other two types of cells and thus can be detected by the fPCA based score plots, though less metastatic MDA-MB-468 TNBC cells and MCF-10A normal breast cells are more mechanically similar and difficult to distinguish. This might have negative implications for early cancer detection of less metastatic TNBC cells.

It is noted that the clusters constructed using creep compliance data for a longer time period (up to 0.8 s) show even lower discrimination power between MCF-10A normal breast cells and less metastatic MDA-MB-468 TNBC cells than the corresponding fPCA focusing on earlier stage data (up to 0.4 s). This might highlight the importance of considering the timing of cell shear responses relative to their viscoelasticity relaxation time.

The relaxation time of MCF-10A and MDA-MB-468 ranged from 0.5 s to 0.7 s (Hu et al., 2018; Onwudiwe et al., 2021; Holen et al., 2023). When the shear data was considered up to 0.4 s, the cell shear responses before cell relaxation time were on focus. The cell shear responses that happened around or earlier than their viscoelasticity relaxation time could be more elastic because viscosity has a lagged effect compared to modulus in the viscoelasticity behavior of cells. The cell cytoskeleton needs time to reorganize to show full and complicated viscoelastic responses. Therefore, more elasticity-driven earlier-stage data can more easily show the elastic modulus difference of the cells than the data from the longer time period.

4.3. Comparison of functional principal component analysis and linear viscoelastic modeling

Fig. 8 shows the PC1 scores of nucleus and cytoplasm regions of the studied three types of cells compared to their corresponding average modulus and viscosity estimated using a 3-element generalized Maxwell viscoelastic model in Fig. 2(a). Note the sample size n = 129 for MCF-10A nucleus region, n = 168 for MCF-10A cytoplasm region, n = 198 for MDA-MB-468 nucleus region, n = 167 for MDA-MB-468 cytoplasm region, n = 106 for MDA-MB-231 nucleus region, and n = 129 for MDA-MB-231 cytoplasm region.

The PC1 scores of MCF-10A normal breast cells, less metastatic MDA-MB-468 TNBC cells, and highly metastatic MDA-MB-231 TNBC cells are

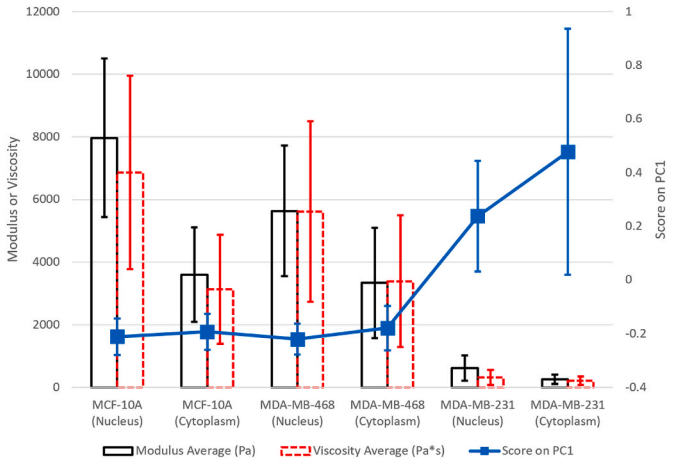


Fig. 8. The PC1 scores of nucleus and cytoplasm regions of normal breast cells, less metastatic MDA-MB-468 TNBC cells, and highly metastatic MDA-MB-231 TNBC cells MCF-10A compared to their corresponding average modulus and viscosity estimated using linear viscoelastic modeling. Error bar shows the standard deviation.

83% negatively correlated with the average moduli and 85% negatively correlated with the average viscosities using the viscoelastic modeling curve fitting approach (Hu et al., 2018; Onwudiwe et al., 2021). This suggests that the functional principal component analysis based PC1 score, as a cell overall compliance measure, is directly correlated with cell viscoelasticity and the related cancer malignancy.

The PC1 scores of the nucleus region are statistically significantly smaller than those of the cytoplasm region ($p < 0.05$) for all three types of cells, indicating that the nucleus region is much stiffer than the cytoplasm region, although with high coefficient of variation in the cytoplasm region. These results are consistent with the observations of the Young's modulus of the cytoplasm and the nuclei of the three cell lines obtained using viscoelastic modeling in a prior study by our research group (Hu et al., 2018).

The PC1 scores either between MCF-10A normal breast cells and highly metastatic MDA-MB-231 TNBC cells or between less metastatic MDA-MB-468 TNBC cells and highly metastatic MDA-MB-231 TNBC cells are all statistically significant ($p < 0.05$ for both nucleus and cytoplasm), though the difference of the PC1 scores between MCF-10A and MDA-MB-468 were not statistically significant ($p = 0.20$ for cytoplasm and $p = 0.31$ for nucleus). This might indicate potential challenges in differentiating early stage of cancer purely based on the mean value of PC1 scores. Though the cluster of PC1 scores, as shown in Fig. 7, bring new perspectives for distinguishing early stage of cancer by introducing other features of the PC1 scores such as distribution, density, and size etc. in addition to the center position/mean position.

While the viscoelastic modeling of the properties of the cells classifies their different states into either metastatic or non-metastatic, it often relies on human subjective judgement for model selection. This poses some limitations in its objective use for the detection of early-stage triple negative breast cancer. On the other hand, the use of fPCA might provide more unbiased, effective, and data-driven classification of cells independent of cellular response and characteristic viscoelastic model fit.

4.4. Correlation between first functional principal component and actin cytoskeletal structure

The first PC measures the cell overall creep compliance level which is the inverse of cell stiffness. Actin cytoskeletal structure that plays a crucial role in cell stiffness can be examined using immunofluorescence microscopy. It is worthwhile to compare the actin cytoskeletal structure of highly metastatic MDA-MB-231 TNBC cells that are easily detectable by the first PC, with the normal MCF-10A breast cells to reveal potential correlation.

Fig. 9 shows the immunofluorescence image of a highly metastatic MDA-MB-231 TNBC cell compared with an MCF-10A normal breast cell. In the normal MCF-10A breast cell, a tightly compacted actin cytoskeletal network can be observed. Conversely, the highly metastatic MDA-MB-231 TNBC cell displays a more scattered arrangement of actin filament bundles. This remarkable difference in the actin filament bundle's density and structure is consistent to the comprehensive confocal immunofluorescence microscopy studies of MDA-MB-231 highly metastatic TNBC cells and MCF-10A normal breast cells that have been done in our group (Hu et al., 2018; Onwudiwe et al., 2021).

The significant decrease of density from normal cells to highly metastatic cells is consistent with the trend of the first PC scores in Fig. 8. The scores on PC1, i.e. overall compliance level, were observed to significantly increase from normal MCF-10A breast cells to highly metastatic MDA-MB-231 TNBC cells. This significantly increased compliance could help cancer cells to easily squeeze into much smaller pores/capillaries to facilitate their migration to other organs. (Paul et al., 2017; Leuschner et al., 2006).

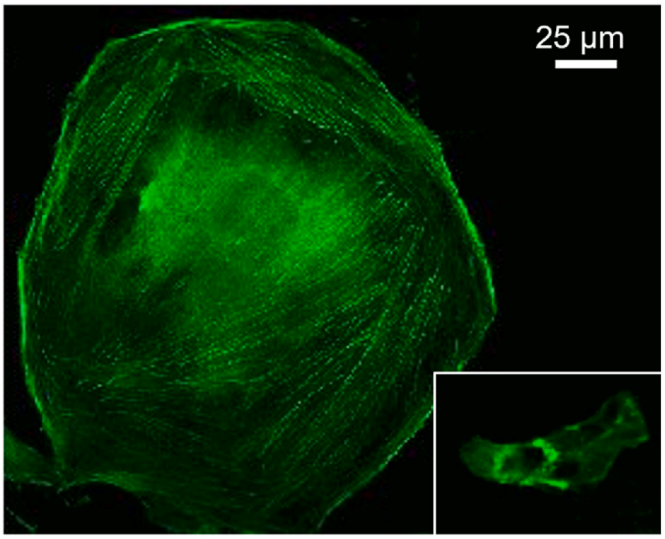


Fig. 9. Immunofluorescence image of a highly metastatic MDA-MB-231 TNBC cell with an MCF-10A normal cell (inset).

4.5. Implications

This novel fPCA data science method can be potentially utilized to detect highly metastatic breast cancer malignancies due to fPCA's unbiased nature compared to viscoelastic models. The fCPA utilizes its data-driven technique to capture underlying data structure without making strong assumptions about the underlying processes, thus predicating outcomes without a specific prior model for cellular properties. It confirms objectively that less metastatic TNBC cells are mechanically and visco-elastically similar to the normal breast cells. However, we might need to explore alternative methods to detect cancer during the early stages of cancer development.

Another significant advantage of employing fPCA is its quick, easy, interpretable, and automatic nature. By circumventing viscoelastic modeling related primary regime determination, model selection, and associated nonlinear model fitting, this approach minimizes potential sources of variance, convergence issues, and time-consuming and costly measurements of mechanical properties such as modulus and viscosity. The automatable potential of this method might be suitable for future microfluidic tumor-on-a-chip systems.

The use of fCPA might also greatly improve the amount of useable data for the classification of cells. This would further enhance the development of mechanical biomarkers for the detection of challenging cancers such as TNBC, reducing computational cost and improving efficiency. The need for improved techniques to capture early deviations in normal cellular behavior necessitates the use of fPCA which represents a novel approach to better utilize unique disparities in cellular behavior to characterize cell states and develop biomarkers for early detection of diseases.

This study provides a strong connection between creep compliance-based data science and traditional cell viscoelasticity modeling for shear assay experiments. The study can be extended to study different biomechanics properties due to different cell malignancy statuses, different cell types, and different cell-extracellular fluid environments. This interdisciplinary approach to biomechanics allows for a more comprehensive understanding of cell deformation under shear stresses, potentially leading to more effective solutions for future identification of disease diagnostics and treatment based on biomechanics biomarkers.

5. Conclusions

This paper presents a data science method for the unbiased analysis of the *in-situ* shear responses of non-tumorigenic breast cells and breast cancer cell lines at different stages of cancer development. The method involved novel fPCA, in addition to more established protocols that use shear assay experiments and DIC techniques. This offers a promising avenue for the development of mechanical biomarkers and methods for cancer diagnosis. The method also uncovers valuable insights into the dis-similarity and similarity of viscoelastic properties of breast cells at different stages of tumor progression. The correlations between cell mechanical responses and cancer malignancy are explored before discussing the implications of the current work for early cancer diagnostics and therapies.

CRediT authorship contribution statement

Jolene Cao: Conceptualization, Data curation, Formal analysis, Investigation, Methodology, Software, Validation, Visualization, Writing – original draft, Writing – review & editing. **Killian Onwudiwe:** Data curation, Investigation, Validation, Writing – review & editing. **Jingjie Hu:** Data curation, Investigation, Validation, Writing – review & editing. **Meenal Datta:** Funding acquisition, Validation, Writing – review & editing. **Wole Soboyejo:** Conceptualization, Funding acquisition, Project administration, Resources, Supervision, Writing – review & editing.

Declaration of competing interest

The authors declare that they have no known competing financial interests or personal relationships that could have appeared to influence the work reported in this paper.

Acknowledgments

This work was supported by the National Cancer Institute NIH/NCI K22 CA258410 (to MD), the Worcester Polytechnic Institute (JC, KO, WS), North Carolina State University (JH), and the SUNY Polytechnic Institute (WS).

Data availability

Data will be made available on request.

References

Aneiros, G., Cao, R., Fraiman, R., Genest, C., Vieu, P., 2019. Recent advances in functional data analysis and high-dimensional statistics. J. Multivariate Anal. 170, 3–9.

Ani, C.J., Obayemi, J.D., Uzonwanne, V.O., Danyuo, Y., Odusanya, O.S., Hu, J., Malatesta, K., Soboyejo, W.O., 2019. A shear assay study of single normal/breast cancer cell deformation and detachment from poly-di-methyl-siloxane (PDMS) surfaces. J. Mech. Behav. Biomed. Mater. 91, 76–90.

Calzado-Martin, A., Encinar, M., Tamayo, J., Calleja, M., Paulo, A.S., 2016. Effect of actin organization on the stiffness of living breast cancer cells revealed by peak-force modulation atomic force microscopy. ACS Nano 10 (3), 3365–3374.

Cao, Y., Bly, R., Moore, W., Gao, Z., Cuitino, A.M., Soboyejo, W., 2006. Investigation of the viscoelasticity of human osteosarcoma cells using a shear assay method. J. Mater. Res. 21 (8), 1922–1930.

Chu, T.C., Ranson, W.F., Sutton, M.A., Peters, W.H., 1985. Applications of digital-image-correlation techniques to experimental mechanics. Exp. Mech. 25, 232.

Cooke, B.M., Usami, S., Perry, I., Nash, G.B., 1993. A simplified method for culture of endothelial-cells and analysis of adhesion of blood cells under conditions of flow. Microvasc. Res. 45 (1), 33–45.

Dao, M., Lim, C.T., Suresh, S., 2003. Mechanics of the human red blood cell deformed by optical tweezers. J. Mech. Phys. Solid. 51 (11–12), 2259–2280.

Driscoll, M.K., Zaritsky, A., 2021. Data science in cell imaging. Journal of Cell Science 134 (7).

Forgacs, G., Foty, R., Shafrir, Y., Steinberg, M., 1998. Viscoelastic properties of living embryonic tissues: a quantitative study. Biophys. J. 74, 2227.

Guilak, F., Tedrow, J., Burgkart, R., 2000. Viscoelastic properties of the cell nucleus. Biochem. Biophys. Res. Commun. 269 (3), 781–786.

Holen, L., Onwudiwe, K., Najera, J., Zarodniuk, M., Obayemi, J., Soboyejo, W.O., Datta, M., 2023. Shear assay protocol for the determination of single-cell material properties. JoVE J. 195, e65333.

Hu, J., Zhou, Y., Obayemi, J.D., Du, J., Soboyejo, W.O., 2018. An investigation of the viscoelastic properties and the actin cytoskeletal structure of triple negative breast cancer cells. J. Mech. Behav. Biomed. Mater. 86, 1–13.
Hurvich, C.M., Tsai, C.L., 1989. Regression and time series model selection in small samples. Biometrika 76 (2), 297–307.
Jain, R.K., Martin, J.D., Stylianopoulos, T., 2014. The role of mechanical forces in tumor growth and therapy. Annu. Rev. Biomed. Eng. 16, 321–346.
Ji, Y, Lotfollahi, M, Wolf, F.A., Theis, F.J., 2021. Machine learning for perturbational single-cell omics. Cell Systems 12 (6), 522–537.
Ketene, A.N., Schmelz, E.M., Roberts, P.C., Agah, M., 2012. The effects of cancer progression on the viscoelasticity of ovarian cell cytoskeleton structures. Nanomed. Nanotechnol. Biol. Med. 8 (1), 93–102.
Krehbiel, J.D., Lambros, J., Viator, J.A., Sottos, N.R., 2010. Digital image correlation for improved detection of basal cell carcinoma. Exp. Mech. 50, 813–824.
Leuschner, C., Kumar, C.S.S.R., Hansel, W., Soboyejo, W., Zhou, J., Hormes, J., 2006. LHRH-conjugated magnetic iron oxide nanoparticles for detection of breast cancer metastases. Breast Cancer Res. Treat. 99 (2), 163–176.
Li, H., Staudenmayer, J., Carroll, R.J., 2014. Hierarchical functional data with mixed continuous and binary measurements. Biometrics 70 (4), 802–811.
Liu, X., Fang, J., Huang, S., Wu, X., Xie, X., Wang, J., Liu, F., Zhang, M., Peng, Z., Hu, N., 2021. Tumor-on-a-chip: from bioinspired design to biomedical application. Microsyst. Nanoeng. 7 (50), 1–23.
Matthews, B., Overby, D., Alenghat, F., Karavitis, J., Numaguchi, Y., Allen, P., Ingber, D., 2004. Mechanical properties of individual focal adhesions probed with a magnetic microneedle. Biochem. Biophys. Res. Commun. 313, 758.
Mayro, E.L., Wang, M., Elze, T., Pasquale, L.R., 2020. The impact of artificial intelligence in the diagnosis and management of glaucoma. Eye 34 (1), 1–11.
Moccia, C., Haase, K., 2021. Engineering breast cancer On-chip—Moving toward subtype specific models. Front. Bioeng. Biotechnol. 9 (694218), 1–20.
Nagelkerke, A., Bussink, J., Rowan, A.E., Span, P.N., 2015. The mechanical microenvironment in cancer: how physics affects tumours. Semin. Cancer Biol. 35, 62–70.
Onwudiwe, K., Hu, J., Obayemi, J., Uzonwanne, V., Ani, C., Nwazojie, C., Onyekanne, C., Ezenwafor, T., Odusanya, O., Soboyejo, W., 2021. Actin cytoskeletal structure and the statistical variations of the mechanical properties of non-tumorigenic breast and triple-negative breast cancer cells. J. Mech. Behav. Biomed. Mater. 119, 104505.
Pan, B., 2018. Digital image correlation for surface deformation measurement: historical developments, recent advances and future goals. Meas. Sci. Technol. 29 (82001).
Pan, B., Qian, k., Xie, H., Asundi, A., 2009. Two-dimensional digital image correlation for in-plane displacement and strain measurement: a review. Meas. Sci. Technol. 20, 062001.
Paul, C.D., Mistriotis, P., Konstantopoulos, K., 2017. Cancer cell motility: lessons from migration in confined spaces. Nat. Rev. Cancer 17 (2), 131–140.
Sang, P., Wang, L., Cao, J., 2017. Parametric functional principal component analysis. Biometrics 73, 802–810.
Takada, J., Hamada, K., Zhu, X., Tsuboko, Y., Iwasaki, K., 2023. Biaxial tensile testing system for measuring mechanical properties of both sides of biological tissues. J. Mech. Behav. Biomed. Mater. 146, 106028.
Tseng, Y., Kole, T.P., Wirtz, D., 2002. Micromechanical mapping of live cells by multiple particle-tracking microrheology. Biophys. J. 83 (6), 3162–3176.
VanKooten, T.G., Schakenraad, J.M., VanDerMei, H.C., Busscher, H.J., 1992. Development and use of a parallel plate flow chamber for studying cellular adhesion to solid-surfaces. J. Biomed. Mater. Res. 26 (6), 725–738.
Wang, J.L., Chiou, J.M., Muller, H.G., 2016. Functional data analysis. Annu. Rev. Stat. Appl. 3, 257–295.
Wirtz, D., 2009. Particle-tracking microrheology of living cells: principles and applications. Annu. Rev. Biophys. 38, 301–326.
Wu, H., Kuhn, T., Moy, V., 1998. Mechanical properties of l929 cells measured by atomic force microscopy: effects of anticytoskeletal drugs and membrane crosslinking. Scanning 20 (389).
Yamada, S., Wirtz, D., Kuo, S., 2000. Mechanics of living cells measured by laser tracking microrheology. Biophys. J. 78 (1376).
Yang, J., Bhattacharya, K., 2019. Augmented lagrangian digital image correlation. Exp. Mech. 59, 187–205.
Zhang, X., Karim, M., Hasan, M.M., Hooper, J., Wahab, R., Roy, S., Al-Hilal, T.A., 2022. Cancer-on-a-Chip: models for studying metastasis. Cancers 14 (648), 1–23.